

pubs.acs.org/JACS Article

# Controlling the Self-Assembly of New Metastable Tin Vanadium Selenides Using Composition and Nanoarchitecture of Precursors

Dmitri Leo Mesoza Cordova, Taryn Mieko Kam, Renae N. Gannon, Ping Lu, and David C. Johnson\*



Cite This: J. Am. Chem. Soc. 2020, 142, 13145-13154

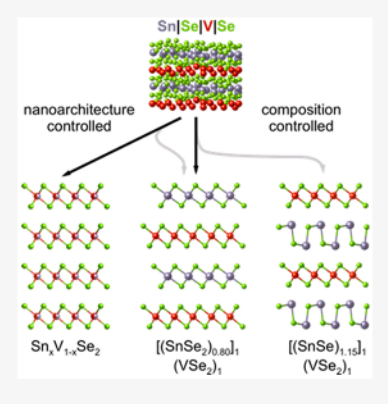


**ACCESS** I

Metrics & More

Article Recommendations

ABSTRACT: In solid-state chemistry, the direct reaction of elements at low temperatures is limited by low solid-state interdiffusion rates. This and the limited number of processing parameters often prevent the synthesis of metastable compounds. Precisely controlling the number of atoms and nanoarchitecture of layered elemental precursors enabled the selective synthesis of two closely related metastable tin vanadium selenides via near-diffusionless reactions at low temperatures. Although the nanoarchitectures of the precursors required to form  $[(SnSe_2)_{0.80}]_1(VSe_2)_1$  and  $[(SnSe)_{1.15}]_1(VSe_2)_1$  are very similar, controlling the local composition of the SnlSe layers in the precursors enables the selective synthesis of either compound. The metastable alloy  $Sn_xV_{1-x}Se_2$  was preferentially formed over  $[(SnSe_2)_{0.80}]_1(VSe_2)_1$ , which has the identical composition, by modifying the nanoarchitecture of the precursor. Ex situ in-plane X-ray diffraction and X-ray reflectivity collected as a function of annealing temperature provided information on lateral and perpendicular growth of  $[(SnSe_2)_{0.80}]_1(VSe_2)_1$ . The presence of Laue oscillations throughout the self-assembly provided atomic-scale information on the thickness of the  $[(SnSe_2)_{0.80}]_1(VSe_2)_1$  domains, giving insights



into the self-assembly process. A reaction mechanism is proposed and used to rationalize how composition and nanoarchitecture control the reaction pathway through the free energy landscape.

#### ■ INTRODUCTION

Molecular synthesis is powerful, with chemists being able to perform total syntheses of complex molecules through a series of carefully designed steps beginning from simple precursors. Several important factors have contributed to the development and success of this field. One factor is the ability to predict the structure of potential kinetically stable compounds using simple bonding rules (the octet rule and the 18-electron rule).2,3 A second factor is the diversity of reagents and catalysts that can be used to transform a single functional group, allowing a reaction to be possible for a large number of substrates. A third factor is the typically homogeneous nature of reacting systems, where reactants dissolve in solvents while maintaining their structure. Most of the structure of the different reactants is preserved in the product molecules, as targeted reactions break and make specific bonds. NMR and other spectroscopies give detailed information about speciation, enabling the kinetics of the transformation from reactants to products to be investigated.<sup>4,5</sup> This has enabled molecular chemists to develop rules based on reaction mechanisms to modify reaction parameters to control reaction pathways.6 Because intermediates in a multistep synthesis can be purified, a sequence of specific reactions can be planned using retrosynthetic analysis to synthesize complicated molecules.

In contrast, solid-state synthesis is considered "as much art as science", because the process is mainly experience- and

intuition-driven.8 This reflects important differences between the synthesis of extended structures and molecules. For example, it is much more challenging to predict the structure of potential products, because many metallic elements can have a variety of oxidation states and coordination numbers.9 The formation of an extended structure also involves the repeated formation of specific bonds to form crystals with macroscopic amounts of atoms. This self-assembly of the crystal structure cannot be done using stepwise reactions. Hence, synthesis approaches are less developed and the analytical techniques used to follow reactions often require specialized instrumentation. 10 While the synthesis approach of extended solids using fluids (fluxes, mineralizers, or supercritical fluids) as solvents is similar in many respects to molecular synthesis, 11-13 the reactants typically do not maintain their structure upon dissolution, and very little is typically known about the speciation that occurs in the liquid phase. 14 Spectroscopy and other reaction monitoring methods are also more difficult to implement due to typically higher reaction temperatures,

Received: May 19, 2020 Published: June 30, 2020





opaque fluid phases, and more challenging NMR nuclei. 15,16 Rapidly developing in situ techniques such as transmission electron microscopy and pair distribution function analysis from total scattering can provide insight into compound formation at the atomic level. 17-25 Diffusion is the rate-limiting step in the direct reaction of solids at high temperature, where reactions occur at the interfaces between particles. Because many different interfaces with different crystallographic orientations are reacting between different elements (A-B, B-C, A-C), different reactions will be occurring at different interfaces forming different products at different rates.<sup>27</sup> Most analytical approaches only provide the sum of all of these reactions, making kinetic studies challenging. In most reactions to form extended solids, high temperatures and long times are typically used, resulting in the formation of only thermodynamically stable compounds. 28,29 While the importance of solid-state reaction mechanisms to develop kinetically controlled synthesis approaches has been recognized, the field remains understudied. 30,31

In the field of 2D materials, there is significant interest in the synthesis of heterostructures, especially those containing layered dichalcogenides because of their diverse properties and exfoliable nature due to weak van der Waals interactions between strongly bonded Se-M-Se layers.<sup>32</sup> The system explored here,  $[(SnSe_2)_{1+\delta}]_1(VSe_2)_1$ , is interesting because the phase diagram of Sn-V-Se contains only one ternary equilibrium phase, SnVSe<sub>3</sub>, the misfit layer compound  $(SnSe)_1(VSe_2)_1$ . The metastable heterostructure  $[(SnSe_2)_{1+\delta}]_1(VSe_2)_1$  lies on the tie line connecting  $SnSe_2$ and VSe<sub>2</sub>. The misfit parameter,  $1+\delta$ , reflects the difference in the in-plane unit cell size of between the two layers in the heterostructure<sup>34</sup> and is equivalent to the number of SnSe<sub>2</sub> unit cells per VSe2 unit cell. There have been no reported studies exploring the formation of  $Sn_xV_{1-x}Se_2$  solid solutions; however, the large difference in a-axis lattice parameters (3.356 Å for VSe<sub>2</sub> and 3.811 Å for SnSe<sub>2</sub>)<sup>35,36</sup> suggests that there is limited solid solubility.<sup>37</sup> The  $[(SnSe_2)_{1+\delta}]_1(VSe_2)_1$ heterostructure and the  $Sn_xV_{1-x}Se_2$  solid solution with  $x \sim$ 0.43 targeted here both cannot be synthesized using a classical high temperature solid-state synthesis route.

Here we use precursors made of a repeating sequence of Snl SelVISe elemental layers to selectively form the metastable solids  $[(SnSe_2)_{0.80}]_1(VSe_2)_1$  and  $Sn_xV_{1-x}Se_2$  at low reaction temperatures. The precursors were designed to have different nanoarchitectures, defined as the sequence and thicknesses of the elemental layers deposited. While the layer sequence is the same, the modulation length of precursors I and II differ by a factor of 2. X-ray reflectivity and X-ray diffraction (specular and in-plane) were used to follow the self-assembly of  $[(SnSe_2)_{0.80}]_1(VSe_2)_1$ . Laue oscillations observed in the XRR patterns enable us to determine the number of unit cells of  $[(SnSe_2)_{0.80}]_1(VSe_2)_1$  perpendicular to the substrate as a function of annealing temperature. In-plane XRD patterns enable us to independently follow the lateral growth of SnSe<sub>2</sub> and VSe<sub>2</sub>. This data was used to develop an atomic scale picture of the reaction mechanism. The proposed reaction mechanism was tested by the different nanoarchitecture of precursor II, which formed the new metastable alloy, Sn<sub>x</sub>V<sub>1-x</sub>Se<sub>2</sub>. Using an energy landscape, we rationalized why local composition and nanoarchitecture allowed us to discriminate between different reaction pathways.

## **■ EXPERIMENTAL SECTION**

Thin film multilayer precursors were deposited on (100) oriented Si wafers with native oxide using a custom-built high vacuum physical vapor deposition (PVD) chamber with pressures maintained below 2  $\times~10^{-7}$  Torr. Se (Alfa-Aesar, 99.999%) was deposited using a Knudsen effusion cell, while V (Alfa-Aesar, 99.7%) and Sn (Alfa-Aesar, 99.98%) were deposited using 6 keV electron beam guns. More detailed information about the instrument setup is found elsewhere. The thickness of each element deposited at each step was monitored by quartz crystal microbalances found above each elemental source. A custom-made LabView code controls the opening and closing of pneumatic shutters to control the sequence and amount of each element deposited.

The areal density (in atoms/Å<sup>2</sup>) of each element was measured using X-ray fluorescence (XRF) on a Rigaku ZSX Primus II spectrometer. For each sample, the background signal was subtracted using the actual measurement from blank substrates as described by Hamann and co-workers.<sup>39</sup>

Precursors were annealed on a hot plate in a drybox with an inert atmosphere (O<sub>2</sub> < 0.8 ppm). X-ray reflectivity (XRR) and specular Xray diffraction (XRD) patterns were collected on a Bruker D8 diffractometer equipped with Cu K $\alpha$  radiation. One piece of precursor I was annealed for 5 min at various temperatures to determine the processing conditions to form [(SnSe<sub>2</sub>)<sub>0.80</sub>]<sub>1</sub>(VSe<sub>2</sub>)<sub>1</sub>. A second piece of precursor I and precursor II were annealed at the optimum processing conditions. The Kiessig and Laue oscillations observed in the XRR pattern were used to calculate the thickness of the film via a modified form of Bragg's Law and the size of the coherently scattering domains, respectively. Grazing incidence in-plane diffraction (GIXRD) patterns were collected on a Rigaku Smartlab diffractometer also equipped with Cu Klpha radiation. A model for the position of the atomic planes along the c axis was optimized by Rietveld refinement of the specular X-ray diffraction patterns using the GSAS-II. 40 LeBail fitting of the in-plane X-ray diffraction using the FullProf Suite was used to refine lattice parameters. 41

A thin cross-section of the film was prepared with an FEI Helios NanoLab 600i DualBeam FIB-SEM using standard lift-out procedures. Scanning transmission electron microscopy data was collected on an FEI Titan G2 80-200 scanning transmission electron microscope (STEM) with a Cs probe corrector and ChemiSTEM technology (X-FEG and SuperX EDS with four windowless silicon drift detectors) operated at 200 kV. High angle annular dark field (HAADF) images were taken with an electron probe of size (fwhm) of about 0.13 nm, current of ~75 pA, convergence angle of 18.1 mrad, and using an annular dark-field detector with a collection range of 60–160 mrad.

#### RESULTS

Two multilayer precursors (I and II) with repeating structure SnlSelVlSe were deposited. The lattice parameters of bulk VSe<sub>2</sub> and SnSe2 were used to calculate the required number of atoms in each SnlSelVlSe sequence to form Se-M-Se trilayers of both VSe<sub>2</sub> and SnSe<sub>2</sub>. 36,42 Precursor I used these targets and the SnISelVISe sequence was repeated 41 times. Precursor II contained the SnlSelVlSe sequence repeated 82 times, with each sequence containing one-half the number of atoms needed to form each Se-M-Se trilayer. The two precursors contain the same number of atoms but with a different nanoarchitecture. The total number of atoms of Sn, V, and Se per Å<sup>2</sup> (areal density) were measured using XRF and are summarized in Table 1 along with the targeted values. The measured values of Sn and V for both precursors are within the error of the target amounts. Assuming a single-phased heterostructure product forms and that the excess/vacancies of Se is evenly distributed among the two phases, the precursor I stoichiometry is [(SnSe<sub>2</sub>)<sub>0.78</sub>]<sub>1</sub>(VSe<sub>2</sub>)<sub>1</sub> and precursor II stoichiometry is [(SnSe<sub>2,3</sub>)<sub>0.78</sub>]<sub>1</sub>(VSe<sub>2,3</sub>)<sub>1</sub>. In terms of a solid

Table 1. Number of Atoms Per Unit Area Determined Using XRF Compared to Target Values Based on the Lattice Constants of Bulk SnSe<sub>2</sub> and VSe<sub>2</sub>

		total number of atoms $(Å^2)$		
material	repeating units	Sn	V	Se
precursor I	41	3.3(1)	4.3(1)	14.6(4)
precursor II	82	3.13(9)	4.1(1)	16.6(5)
VSe <sub>2</sub> <sup>35</sup>	41	0	4.203(3)	8.406(6)
$SnSe_2$	41	3.256(5)	0	6.52(1)

solution, precursor I's stoichiometry is  $Sn_{0.43}V_{0.57}Se_2$  and precursor II's stoichiometry is  $Sn_{0.43}V_{0.57}Se_{2.29}$ . The limiting reagent in precursor I is Se, and there is enough Se to form 40(1) unit cells of the heterostructure or 80(2) unit cells of the alloy. In precursor II, the rate limiting reagent to form the heterostructure is Sn and there is enough Sn to form 39(1)

unit cells of the heterostructure. With respect to the alloy, the metals are the limiting reagent and there is enough metal to form 79(1) unit cells of  $Sn_xV_{1-x}Se_v$ .

The evolution of a piece of precursor I was followed as a function of annealing temperature using XRF, XRR, and XRD to determine the conditions to form a single-phase  $[(SnSe_2)_{1+\delta}]_1(VSe_2)_1$  sample (Figure 1). The XRR scan (Figure 1b) contains Kiessig fringes from the interference between the front and the back of the deposited film. The spacing of the Kiessig fringes yield a film thickness of 550.8(6) Å, and the angle where the Kiessig fringes can no longer be observed yields a surface roughness of  $\sim$ 6 Å. The number of Kiessig fringes observed before the Bragg maxima from the modulation of the electron density in the precursor is consistent with the presence of 41 repeating sequences of SnlSelVlSe layers. The position of the first two Bragg reflections from the SnlSelVlSe sequence of layers yields a

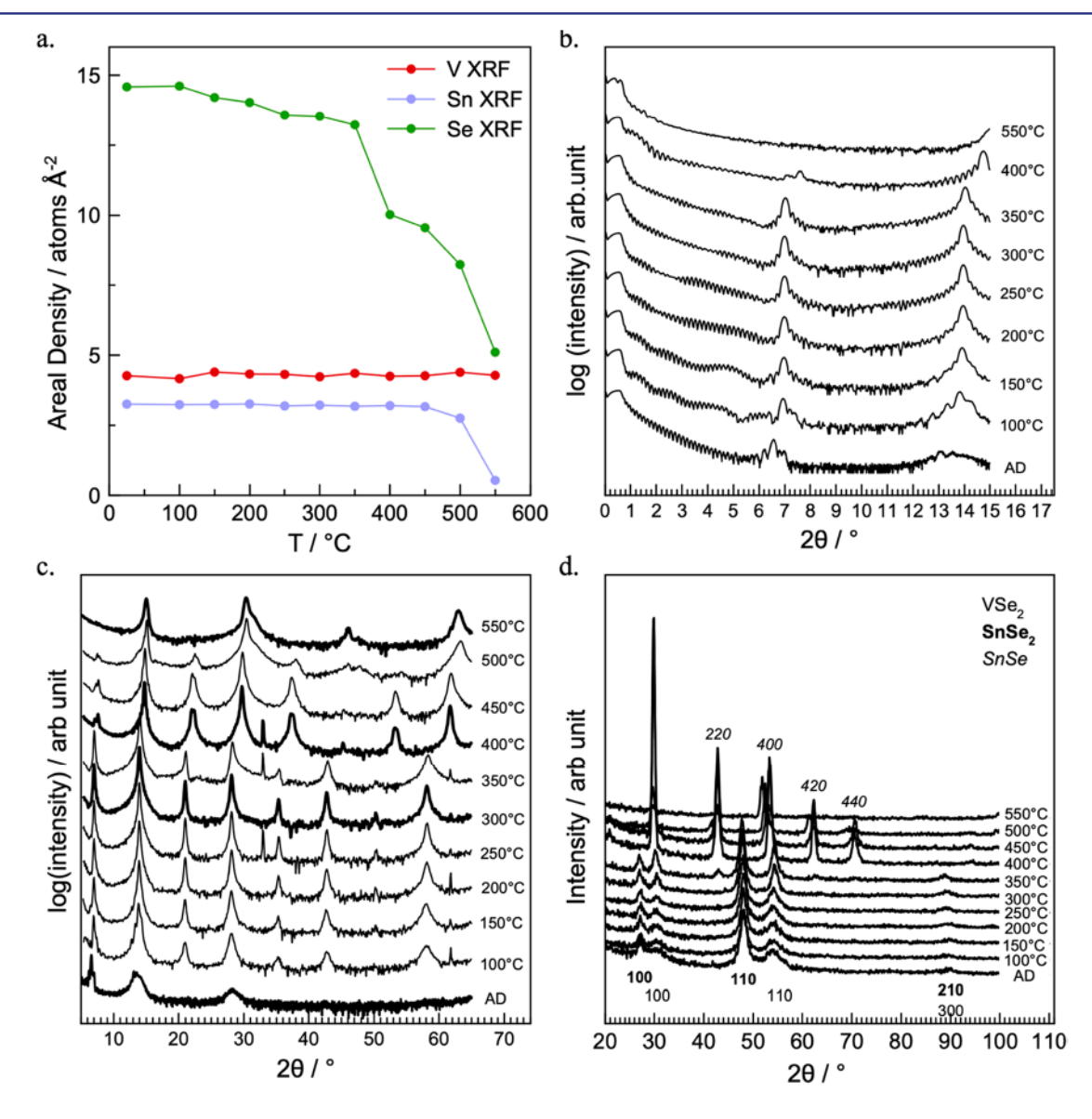


Figure 1. Evolution of Sn|Se|V|Se precursor annealed at different temperature steps. (a) The number of atoms per  $Å^2$  of each element measured by XRF at each temperature step and calculated from the number of unit cells and a-lattice parameters at RT, 250 °C, and 400 °C. (b) X-ray reflectivity patterns showing the evolution of the overall film structure (c) Specular X-ray diffraction showing the evolution of the structure perpendicular to the substrate. (d) Grazing incidence in-plane X-ray diffraction showing the evolution of the structure in the plane parallel to the substrate.

modulation length of 13.5 Å. This is slightly larger than the sum of the c-axis lattice parameters of bulk VSe $_2$  and SnSe $_2$ , 12.247(2) Å, because amorphous layers have a lower density than their crystalline counterparts. There is also a broad maximum at  $\sim 14^\circ$ , suggesting that nucleation and coherent stacking of dichalcogenide layers occurs during deposition. Scherrer analysis of the line width suggests that the thickness of the coherent stacking is only a few layers thick. The XRR and XRF data (Figure 1a,b) indicate that the nanoarchitecture of the precursor is close to what was targeted and resembles the desired product.

The diffraction data (Figure 1c,d) collected on the as deposited precursor is consistent with the XRR discussion. The specular XRD pattern (Figure 1c) contains two narrow Bragg reflections from the repeating SnlSelVlSe sequence of layers and broad reflections from self-assembly occurring during the deposition of the precursor. The broad reflections at  $\sim$ 14° and 28° indicate that coherent domains have formed. The in-plane XRD pattern (Figure 1d) contains hk0 peaks that can be indexed to two hexagonal unit cells, SnSe<sub>2</sub> and VSe<sub>2</sub>, with a-lattice parameters of 3.78(1) and 3.39(1) Å. The peak widths of SnSe<sub>2</sub> is narrower than VSe<sub>2</sub>, indicating that there are larger in-plane grains of SnSe<sub>2</sub> than VSe<sub>2</sub>.

The data collected between 100 °C and 300 °C show that  $[(SnSe_2)_{1+\delta}]_1(VSe_2)_1$  gradually self-assembles during this temperature range. The XRF data (Figure 1a) indicates that there is a small decrease in the amount of Se in this temperature range, which results from evaporation of Se while annealing. The XRR patterns (Figure 1b) contain an additional low frequency Kiessig oscillation due to the growth of an oxide at the surface of the film. The film thickness calculated from the high frequency Kiessig fringes in the XRR indicate that the film thickness gradually decreases as annealing temperature increases, which is a consequence of both the loss of Se and the increasing density of the film. The first two diffraction maxima shift in angle on annealing at 100 °C and then increase in intensity and become narrower as annealing temperature increases. Laue fringes, 44,45 which originate from the finite number of unit cells in the coherently diffracting coherent domains of the film, are clearly visible on the diffraction maxima at 14° and become closer together as the annealing temperature increases. This indicates that the majority of the coherent domains are the identical thickness, which can be calculated from the frequency of the Laue oscillations. During the growth process, the low angle Bragg reflections from the artificial layering of the precursor disappears. The specular XRD patterns (Figure 1c) confirm the formation of  $[(SnSe_2)_{1+\delta}]_1(VSe_2)_1$  and corroborate growth of the coherent domains perpendicular to the substrate. Starting at 100 °C, long-range order starts to develop as additional 00l reflections appear at higher angles. These 00l reflections increase in intensity, reaching a maximum at 250-300 °C. The positions of the 00l Bragg reflections yield a c-axis lattice parameter of 12.69(1) Å, which is slightly larger than the sum of the c-axis lattice parameters of bulk VSe2 and SnSe2, 12.247(2) Å, presumably due to the in-plane lattice mismatch preventing nesting of one constituent layer in the other. Laue oscillations, indicating a common size for the different  $[(SnSe_2)_{1+\delta}]_1(VSe_2)_1$  domains after each annealing temperature, are observed on the first several Bragg reflections and will be discussed more fully in the next paragraph. The in-plane diffraction patterns (Figure 1d) reflect the in-plane crystal growth that also occurs during annealing. The SnSe<sub>2</sub> hk0

reflections exhibited only small changes in peak width and intensity, indicating that most of the SnSe<sub>2</sub> is crystalline as deposited and the crystallite size does not increase during the annealing. The VSe<sub>2</sub> hk0 reflections, however, noticeable increase in peak intensity and decrease in peak width as annealing temperature increases, indicating an increase in the amount of crystalline VSe<sub>2</sub> and growth of the in-plane grain sizes.

The characterization data in this temperature range provide a coherent picture of the self-assembly of  $[(SnSe_2)_{1+\delta}]_1(VSe_2)_1$  from the as-deposited precursor. Figure 2a contains a closer

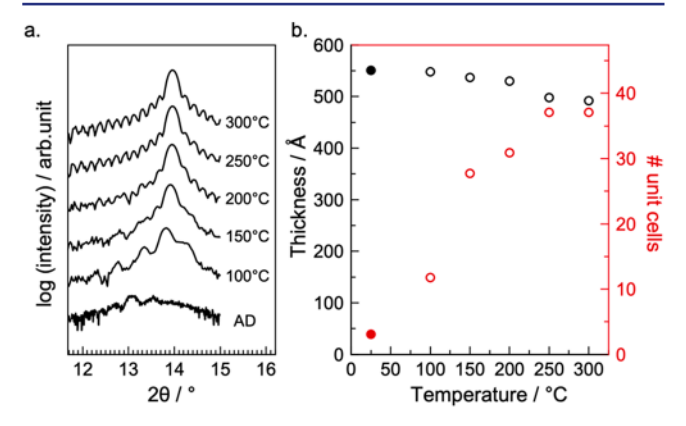


Figure 2. (a) Laue oscillations coming from the coherent film thickness at different temperatures. (b) Kiessig (black circles) and Laue (red circles, left axis) film thickness, and the number of unit cells (red circles, right axis) formed at each annealing temperature. The size of the coherent domain in the as-deposited sample (filled red circle) is estimated from the line width of the 002 reflection.

view of the Laue oscillations visible on the 002 reflection of  $[(SnSe_2)_{1+\delta}]_1(VSe_2)_1$  after each annealing temperature. The presence of these oscillations indicates that a large majority of the suite of  $[(SnSe_2)_{1+\delta}]_1(VSe_2)_1$  domains at each temperature are the identical size and an integral number of unit cells thick, which can be calculated from the spacing of the Laue oscillations. Figure 2b graphs the change in the size of the domains as a function of annealing temperature. At 250 °C, the number of unit cells reach its maximum value of 37. The number of unit cells formed is smaller than expected due to loss of Se and oxidation at the film surface. The overall film thickness (calculated from Kiessig oscillations) decreases by a small amount as the target product grows, due to densification of the film as it self-assembles and loss of some Se. The difference between the total film thickness and the thickness of 37 unit cells of  $[(SnSe_2)_{1+\delta}]_1(VSe_2)_1$  at 250 °C is due to an oxide layer on the surface of the film. The areal density of Se measure using XRF is consistent with that expected for 37 unit cells of  $[(SnSe_2)_{1+\delta}]_1(VSe_2)_1$  at 250 °C (solid green line,

A growth mechanism consistent with the characterization data is shown in Figure 3. The most difficult fact to explain is that the majority of the film consists of domains of  $[(SnSe_2)_{1+\delta}]_1(VSe_2)_1$  that are exactly the same integral number of unit cells throughout the annealing process. One possible explanation is that the coherent domains in the as-deposited film grow out from the substrate film interface as the film is deposited. This would provide a common starting point for all of the domains. The domains would stop growing as the film is deposited because metal atoms would need to diffuse through

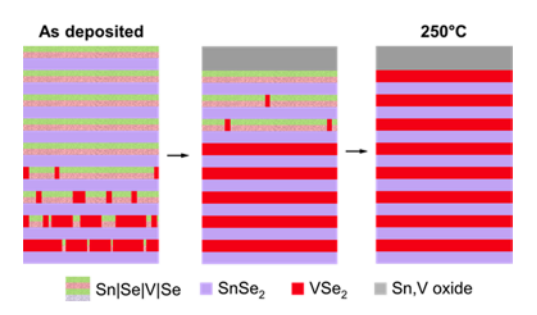


Figure 3. Proposed formation and growth mechanism for  $[(SnSe_2)_{1+\delta}]_1(VSe_2)_1$ .

a thicker layer of amorphous Se and the increasing accumulated roughness as the film becomes thicker would decrease the coherence of the later deposited layers. The inplane diffraction patterns suggest that most of the SnSe<sub>2</sub> forms large 2D grains during the deposition. There are fewer and smaller domains of VSe2 and unreacted VISe layers between the SnSe<sub>2</sub> grains. As the precursor is annealed, the number of unit cells in the coherent domains near the substrate increase and an oxide layer forms at the film surface. The coherent domains grow at the same rates because the diffusion distances for atoms to arrive at the growth fronts are similar as a result of the nanoarchitecture of the precursor. Nucleation of the dichalcogenide takes place at the growth front near small crystallites because heterogeneous nucleation is easier due to the presence of an existing surface. Homogenous nucleation far away from the growth front is unfavorable because it would require the formation of a larger amount of additional surface area. 46 During this process, lateral growth of existing VSe2 layers in the precursor occurs and additional VSe2 layers selfassemble between existing SnSe<sub>2</sub> layers as charge transfer between the layers stabilize the intergrowth. Excess Se diffuses to the surface and evaporates. The difference in the selfassembly behavior of SnSe2 and VSe2 results in an interesting dynamic between lateral and perpendicular growth of  $[(SnSe_2)_{1+\delta}]_1(VSe_2)_1$ . Overall, the formation of the heterostructure is enabled by the low reaction temperatures, which limit long-range diffusion so that the SnlSe and VlSe layers are crystallized without losing the nanoarchitecture of the precursor. The strain energy associated with Sn substituting for V in VSe2 or V substituting for Sn in SnSe2 combined with compositional modulation in the precursor, limit the extent of alloy formation.

Further annealing to 400 °C results in the decomposition of  $[(SnSe_2)_{1+\delta}]_1(VSe_2)_1$  as Se is lost and  $[(SnSe)_{1,15}]_1(VSe_2)_1$ forms. The XRF data (Figure 1a) shows a substantial drop in the number of Se atoms per Å<sup>2</sup> starting at 350 °C. This is close to the decomposition temperature of bulk SnSe<sub>2</sub> to SnSe (340 °C). 47 Changes in the XRR pattern (Figure 1b) from 300 °C to 400 °C demonstrate that the SnSe2 layers have indeed decomposed. The decrease in the Kiessig fringe amplitude point to a change in the density of the film. The number of unit cells also decrease to 32, suggesting that not all of the  $[(SnSe_2)_{1+\delta}]_1(VSe_2)_1$  layers were converted to [(SnSe)<sub>1.15</sub>]<sub>1</sub>(VSe<sub>2</sub>)<sub>1</sub>. This is not at all surprising because SnSe has a higher atomic areal density of Sn than SnSe<sub>2</sub>. The SnSe<sub>2</sub> decomposition does not reduce the number of VSe<sub>2</sub> layers, because VSe<sub>2</sub> is kinetically stable up to 400 °C.<sup>48</sup> The VSe<sub>2</sub> layers that are not in the heterostructure likely exist as small VSe2 grains within the film. The retention of the Kiessig fringes in the XRR pattern show that the film remains smooth

during this transition. The c-axis lattice parameter of 12.02(1) Å after the 400 °C anneal is consistent with previously reported  $[(SnSe)_{1.15}]_1(VSe_2)_1^{.49}$  The odd order reflections are broader than the even order reflections, presumably due to peak splitting from extra planes of  $VSe_2$  separating domains of  $[(SnSe)_{1.15}]_1(VSe_2)_1$  by half of a unit cell's thickness within the interior of the film. The in-plane diffraction data (Figure 1d) supports the formation of  $SnSe.^{49}$  After the 350 °C anneal, hk0 reflections from  $VSe_2$ ,  $SnSe_2$  and SnSe are present. After the 400 °C anneal, the  $SnSe_2$  hk0 reflections are no longer present. The a-axis lattice parameter of the  $VSe_2$  phase is 3.43(1) Å, consistent with previously studied  $[(SnSe)_{1.15}]_1(VSe_2)_1$  ( $VSe_2$ ) a = 3.414(3) Å). SnSe has a square unit cell and an a axislattice parameter of 5.94(1) Å, which is also consistent with previous reports for  $[(SnSe)_{1.15}]_m(VSe_2)_1$  (SnSe a = 5.91-5.92 Å).

The last phase transition involves the disproportionation and subsequent oxidation of  $[(SnSe)_{1,15}]_1(VSe_2)_1$  at temperatures greater than 450 °C, even though the sample was annealed in a drybox with low oxygen concentration. Another dramatic drop in Se atoms per Å<sup>2</sup> is observed during this last transition (Figure 1a). This transition coincides with an increase in oxygen XRF intensity and decrease in Sn atoms per Å<sup>2</sup>. These stoichiometry changes suggest that the disproportionation is accompanied by the oxidation of and/or V and the loss of both Sn and Se through volatile species. The XRR data shows that the film roughness significantly increases. The 00l peaks in the XRD shift to higher angles and broaden starting at 500 °C. Odd order 00l reflections are completely diminished at 550 °C, and what remains are 00l reflections coming from a structure with a c-lattice parameter of 5.90(1) Å, consistent with some nonstoichiometric VSe<sub>2</sub> remaining in the film. 42 At the highest temperature studied, only hk0 reflections (Figure 1d) from two closely related hexagonal lattices are observed, with a-lattice parameters of 3.46 and 3.52 Å, suggesting that the major phase present is  $VSe_2$  with different values of x and y in the formula  $V_{1+x}Sn_vSe_2$ .

A second piece of precursor I was annealed at 250 °C for 5 min based on the annealing data, and its XRR pattern is shown in Figure 4a (black circles). The Laue oscillations around the first-order Bragg maximum are consistent with 39 layers of  $[(SnSe_2)_{1+\delta}]_1(VSe_2)_1$  self-assembling during the anneal. Fewer layers oxidized during this single annealing step compared to the sequential annealing done on the first piece of precursor I. The total thickness determined from the Kiessig fringes is larger than 39 times the unit cell parameter of  $[(SnSe_2)_{1+\delta}]_1(VSe_2)_1$ , as two of the deposited precursor layers did not form the intended product. We modeled the XRR data using the program GenX to calculate the XRR pattern from our proposed structural model.  $^{52}$ 

The calculated pattern, shown in Figure 4a (red line), matches the experimental pattern, and the film parameters in the model are summarized in Table 2. The model contained 39 unit cells of  $[(SnSe_2)_{0.80}]_1(VSe_2)_1$  with atomically smooth interfaces between the constituents, a rough layer of  $SiO_2$  below the  $[(SnSe_2)_{0.80}]_1(VSe_2)_1$  block, and a rough layer of tin/vanadium oxides above it. The thickness of the top oxide layer is approximately equal to that of the two missing unit cells, suggesting that they were mostly lost to oxidation. A thin interdiffusion region was required in the model to match the experimental pattern, which is consistent with a small amount of initially deposited Sn reacting with the  $SiO_2$  surface during deposition.

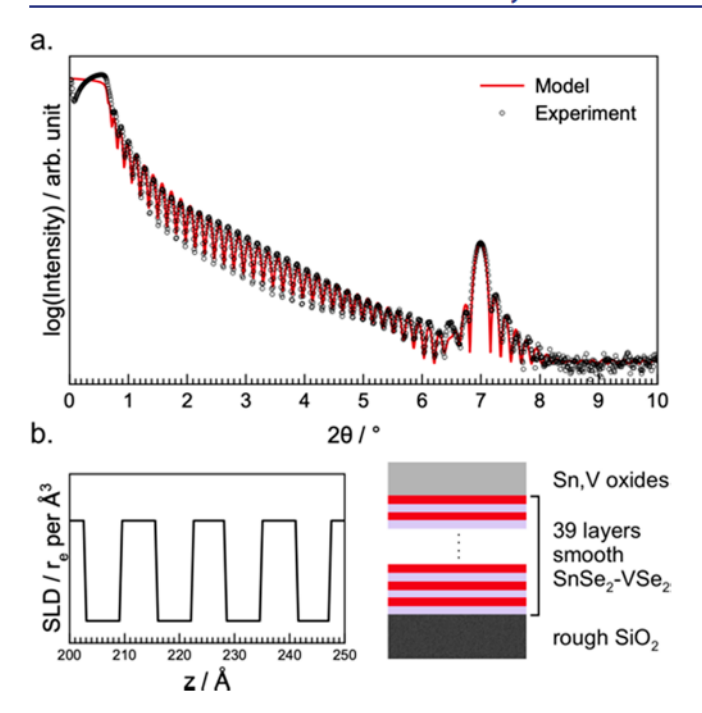


Figure 4. (a) XRR modeling of the optimized [(SnSe<sub>2</sub>)<sub>0.80</sub>]<sub>1</sub>(VSe<sub>2</sub>)<sub>1</sub> heterostructure. (b) Electron density profile and schematic of the film based on the model.

Rietveld analysis of the specular X-ray diffraction of  $[(SnSe_2)_{0.80}]_1(VSe_2)_1$  is shown in Figure 5. Because only 00l reflections are observed, a Rietveld analysis only provides information on the atomic positions of the atomic planes in the heterostructures that are parallel to the substrate. To simplify the analysis, a model with V at zero and Sn at half the c-axis lattice parameter was used, with a mirror plane at the halfway point. The refined V-Se distance of 1.54 Å is close to those observed in other VSe2 heterostructures such as  $[(SnSe)_{1+\delta}]_1(VSe_2)_1(1.48(2) \text{ Å}),^{49} [(PbSe)_{1+\delta}]_1(VSe_2)_1(1.54 \text{ Å}),^{53} [(BiSe)_{1+\delta}]_1(VSe_2)_1(1.52(1) \text{ Å}),^{54} \text{ and bulk } VSe_2(1.57 \text{ Å}),^{54}]_1(VSe_2)_1(1.52(1) \text{ Å}),^{54}]_1(VSe_2)_1(1.52(1) \text{ Å})$ Å).35 The refined Sn-Se distance (1.59 Å) is close to that observed in  $[(SnSe_2)_{1+\delta}]_1(MoSe_2)_1$  (1.57 Å)<sup>55</sup> and bulk  $SnSe_2$ (1.53 Å).36 The refined van der Waals gap of 3.21 Å is larger than those observed in either VSe2 or SnSe2 but smaller than the gap found in  $[(SnSe_2)_{1+\delta}]_1(MoSe_2)_1 (\bar{3}.35(1) \text{ Å}).^{55}$  The large van der Waals gap is a consequence of the large difference between the in-plane lattice parameters of VSe2 and SnSe2, which prevents the Se atoms on either side of the van der Waals gap from nesting in between the Se atoms of the adjacent layers.

A LeBail fit of the in-plane X-ray diffraction data of the second piece of precursor I is shown in Figure 6. All reflections can be indexed as hk0 reflections from two different hexagonal unit cells. The calculated a-axis lattice parameter for the SnSe<sub>2</sub> constituent (3.79(1) Å) is only slightly lower than what is observed for bulk  $\text{SnSe}_2$   $(3.811 \text{ Å})^{36}$  and in

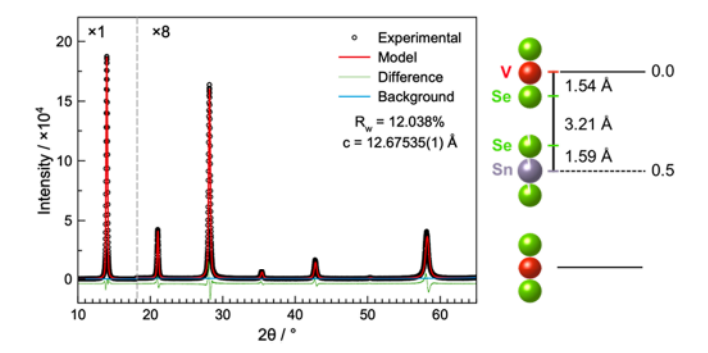


Figure 5. Rietveld refinement result of the specular X-ray diffraction of  $[(SnSe_2)_{0.8}]_1(VSe_2)_1$  and the atomic z-plane model of the average structure.

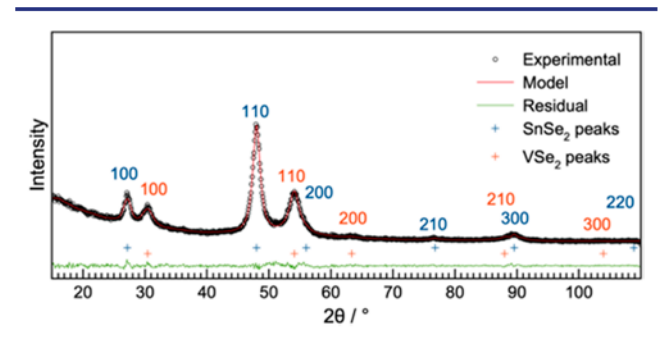


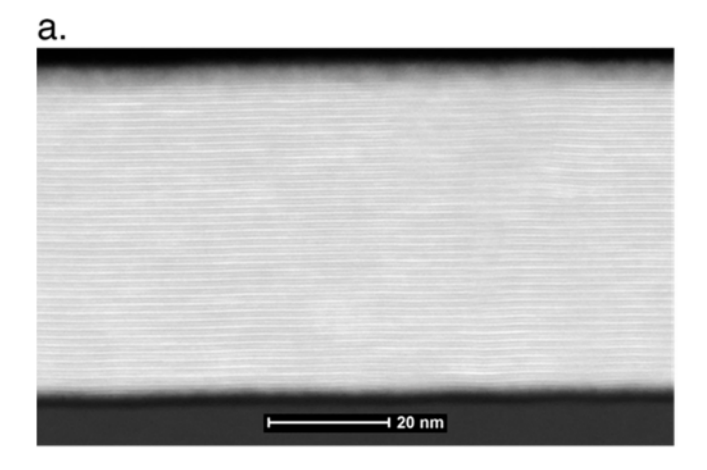
Figure 6. LeBail fit of the grazing incidence in-plane X-ray diffraction pattern of the  $[(SnSe_2)_{0.80}]_1(VSe_2)_1$  heterostructure.

 $[(SnSe)_{1+\delta}]_1(MoSe_2)_1$  (3.81 Å).<sup>55</sup> The calculated *a*-axis lattice parameter for the VSe<sub>2</sub> constituent (3.39(1) Å) is between the bulk value for stoichiometric VSe<sub>2</sub> (3.358 Å)<sup>35</sup> and that reported for  $[(SnSe)_{1+\delta}]_1(VSe_2)_1$  (3.414 Å). Using the in-plane lattice constants, a misfit parameter,  $1+\delta$ , of 0.80(4) is calculated. From this point on, the heterostructure crystallized from the second piece of precursor I is referred to as  $[(SnSe_2)_{0.80}]_1(VSe_2)_1$ .

HAADF-STEM data were obtained on a cross-section of the [(SnSe<sub>2</sub>)<sub>0.80</sub>]<sub>1</sub>(VSe<sub>2</sub>)<sub>1</sub> film from the second annealed piece of precursor I to obtain information about the relative orientation of the dichalcogenide layers. Figure 7a contains an image of the entirety of the film, which shows that the film is homogeneous and smooth, consistent with the modeling of specular XRD and XRR. There are 38 layers of [(SnSe<sub>2</sub>)<sub>0.80</sub>]<sub>1</sub>(VSe<sub>2</sub>)<sub>1</sub> clearly visible, with another layer occasionally found at the top or bottom of the film. A closer look of the film at higher magnification, Figure 7b, contains alternating dark and bright layers that can be identified as VSe2 and SnSe2, respectively, because heavier elements appear brighter in HAADF-STEM data.<sup>56</sup> There are noticeably dark regions between the interfaces of the SnSe2 and VSe2 layers due to the van der Waals gap between the two constituents. The inset of Figure 5b shows a region of layers with high atomic resolution that happens to show zone axis views of both constituent layers.

Table 2. Thin Film Modeling Parameters Obtained from XRR Fitting (FOM = 0.141)

layer	no. of layers	thickness (Å)	density (FU per Å $^3 \times 10^{-2}$ )	roughness (Å)	interdiffusion (Å)
Sn/V oxides	1	24.1(6)	1.6(1)	3.4(4)	-
VSe <sub>2</sub>	39	6.31(4)	1.55(4)	_	_
SnSe <sub>2</sub>		6.38(2)	1.28(4)	-	_
SiO <sub>2</sub>	1	50(20)	1.7(5)	2(1)	4(1)



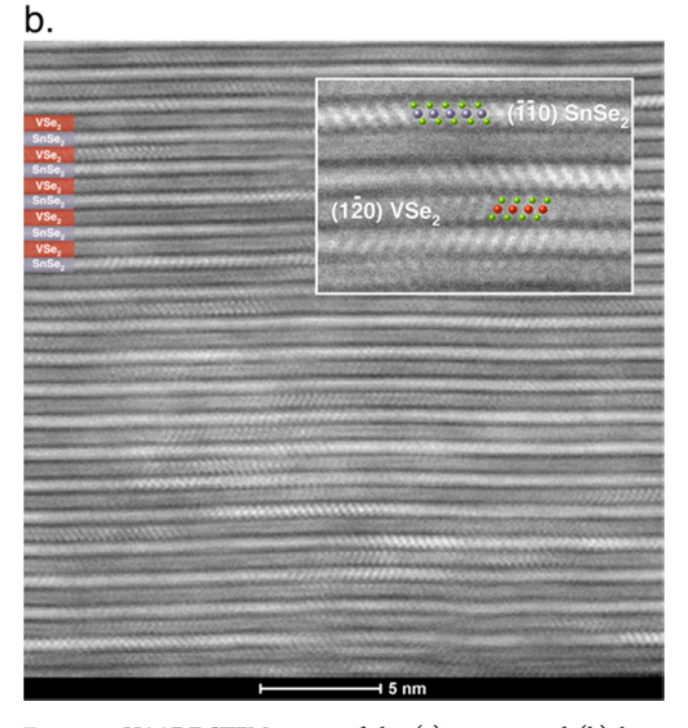


Figure 7. HAADF-STEM image of the (a) entirety and (b) large section of the film shows that it consists of [(SnSe<sub>2</sub>)<sub>0.80</sub>]<sub>1</sub>(VSe<sub>2</sub>)<sub>1</sub>.

Only the \$\langle 110 \rangle\$ and \$\langle 120 \rangle\$ orientations of the two constituents are clearly resolved in the images. Both the VSe2 and SnSe2 layers exhibit octahedral coordination, which is consistent with the bulk structures of SnSe2 and VSe2. It is apparent from the microscopy data that there is a large degree of turbostratic disorder and lack of long-range order in the heterostructure. A close inspection of the entirety of the cross-section reveals that there are no large grains containing multiple repeating units crystallizing with a consistent orientation. Qualitative analysis of Figure 7b gives an estimated grain size of 5 nm, smaller than the grain sizes observed from other heterostructures that have long-range order. These features can be traced to the large lattice mismatch and weak interaction between the constituents.

More information on the elemental distribution of the atoms within the layers was collected by EDX analysis of a small section of the film (Figure 8). The elemental EDX map confirms that there are alternating atomic layers of Sn and V separated by Se. However, there are regions where there is V-intensity in the Sn positions and vice versa. Because the

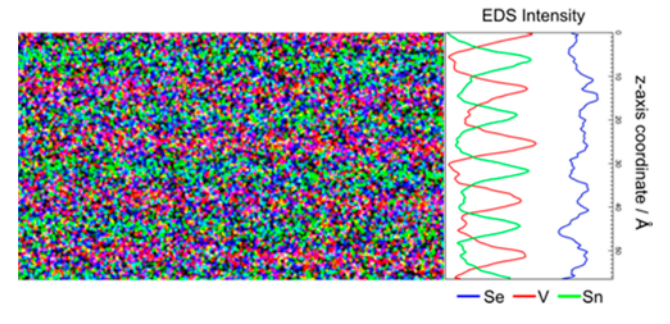


Figure 8. EDX elemental analysis of a section of the film showing atomic plane position of the elements.

unexpected intensities are not uniform across the analyzed region, it is likely due to inhomogeneous cross-substitution (e.g., VSe<sub>2</sub> replacing SnSe<sub>2</sub> or vice versa) across layers rather than homogeneous alloying (e.g., Sn<sub>x</sub>V<sub>1-x</sub>Se<sub>2</sub>) within the layers. Substitutional defects of this type have been observed in nonstoichiometric  $[(SnSe)_{1+\delta}]_1(VSe_2)_1$  when there are deliberate variations in global composition. Homogeneous alloys such as  $[(SnSe)_{1+\delta}]_1(Ta_xV_{1+x}Se_2)_1[(SnSe)_{1+\delta}]_1(V_yTa_{1-y}Se_2)_1$  have clearly resolved V intensity peaks in Ta positions and vice versa. In  $[(SnSe_2)_{0.80}]_1(VSe_2)_1$ , we speculate this result comes from variations in local composition that are difficult to control during the deposition process.

The data presented above on precursor I and the mechanism for growth prompted us to prepare precursor II to probe the relative importance of composition versus nanoarchitecture on product formation. We intended precursor II to have the same composition as precursor I but half the initial modulation length of the deposited sequence of SnlSelVlSe layers. Our question was "what would form from this precursor?". Only short-range diffusion would be required to form the metastable alloy Sn<sub>x</sub>V<sub>1-x</sub>Se<sub>2</sub> and roughly twice that diffusion distance would be required to form the metastable compound [(SnSe<sub>2</sub>)<sub>0.80</sub>]<sub>1</sub>(VSe<sub>2</sub>)<sub>1</sub>. Alternatively, small domains of VSe<sub>2</sub> interwoven with larger domains of SnSe2 might form, or Se might segregate, enabling the thermodynamically stable compound [(SnSe)<sub>1.15</sub>]<sub>1</sub>(VSe<sub>2</sub>)<sub>1</sub> to form. On the basis of the data from precursor I, we expected SnSe2 would nucleate first, but the formation of large in-plane grains of SnSe2 would be inhibited by increasing concentrations of vanadium atoms at the growth front.

Figure 9 contains diffraction data on precursor II. The experimental modulation length of the layering in the asdeposited precursor II was 7.27 Å, close to the c-axis lattice parameters of tin and vanadium diselenides. Figure 9a contains the specular and in-plane diffraction patterns of precursor II after it was annealed at 250 °C. The specular diffraction pattern containing four reflections, that can be indexed as 00l reflections, yields a c-axis lattice parameter of 6.23(1) Å. The 110 reflection from the in-plane diffraction pattern (Figure 9b) of this sample is split, suggesting that the products are a vanadium-rich and a tin-rich dichalcogenide alloy. Vegard's law can be used to estimate the composition of the majority components from the resulting a-axis lattice parameters of a =3.49(1) and 3.75(1) Å. The calculated compositions of the two phases observed are  $Sn_{0.86}V_{0.14}Se_2$  and  $Sn_{0.29}V_{0.71}Se_2.$  We suggest that SnSe2 nucleates and grows but incorporates some V due to the increasing concentration of V at the growth front. The increased concentration of V results in the nucleation of the vanadium-rich dichalcogenide. These events

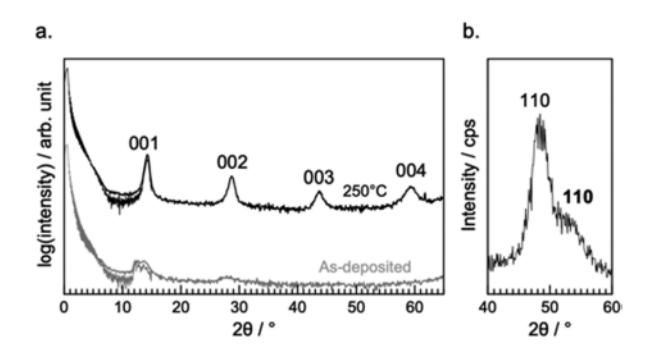


Figure 9. Synthesis of a new  $\mathrm{Sn}_x \mathrm{V}_{1-x} \mathrm{Se}_2$  alloy. (a) Specular X-ray diffraction of a precursor with half the number of required atoms per layer. (b) In-plane X-ray diffraction of the tin and vanadium diselenide alloy showing the presence of alloys with two different values of x.

occur randomly and result in the random intergrowth of the two alloys rather than a precisely layered nanoarchitecture.

### DISCUSSION

Traditional materials synthesis approaches have few parameters that can be used to control a reaction pathway to a specific product, instead relying on changing the system conditions (temperature, pressure, composition) to make the desired product thermodynamically stable. The results presented herein indicate that both the local composition and nanoarchitecture of precursors, which controls the initial distribution of atoms, provide a means to choose between different self-assembly pathways. An energy landscape provides a useful tool to visualize key aspects reaction pathways, and Figure 10

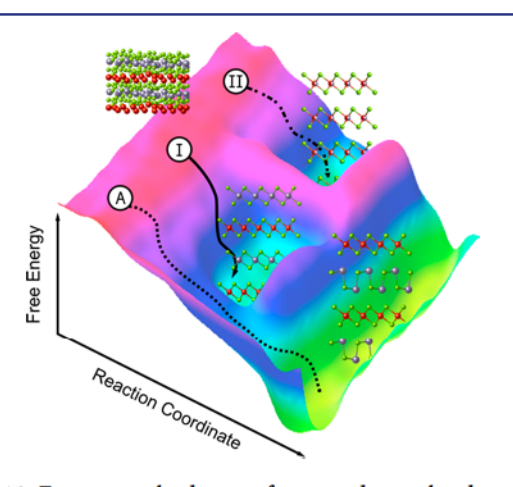


Figure 10. Free energy landscape of tin vanadium selenides.

contains an energy landscape consistent with the results of our study. Figure 10 shows the two kinetically stable phases formed in this study:  $[(SnSe_2)_{0.80}]_1(VSe_2)_1$  and  $Sn_{1-x}V_xSe_2$  exist as local minima and the misfit layer compound  $[(SnSe)_{1.15}]_1(VSe_2)_1$  as the thermodynamic global minimum. Three different starting points are shown, corresponding to precursors I and II, and precursor A containing less Se with the nanoarchitecture designed to form the misfit layer compound  $[(SnSe)_{1.15}]_1(VSe_2)_1$ . As the layers in precursor I self-assemble to form  $[(SnSe)_{11+\delta}]_1(VSe_2)_1$ , the free energy drops as the system falls into the local minima (solid black line from site I). The formation of  $SnSe_2$  during the deposition, facilitated by the local composition and nanoarchitecture of precursor I,

selects this reaction pathway. Precursor II, while having the same overall composition, has a nanoarchitecture that does not provide enough Sn in any single elemental layer to form large grains of SnSe<sub>2</sub>. When SnSe<sub>2</sub> nucleates, the growth front quickly becomes enriched in V, resulting in the formation of the metastable alloy, Sn<sub>1-x</sub>V<sub>x</sub>Se<sub>2</sub> (black dash dot line from site II). Precursor A, reported by Atkins and co-workers, had a nanoarchitecture similar to precursor I, containing alternating Sn- and V-rich layers but ~25% less Se. 49 This precursor forms [(SnSe)<sub>1,15</sub>]<sub>1</sub>(VSe<sub>2</sub>)<sub>1</sub>, as there was not sufficient Se to nucleate SnSe<sub>2</sub> during the deposition. There are large activation barriers between the different products initially formed because it would be necessary to create regions with the local composition required to nucleate the different alternatives, and this would require long-range solid-state diffusion which has a high activation energy.<sup>49</sup> The importance of local composition is also seen in a paper by Falmbigl and coworkers, which involved the reaction of a SnlSelVISe precursor with a nanoarchitecture similar to that of precursors I and A but with an intermediate amount of Se. 60 In this precursor, annealing at 100 °C resulted in the simultaneous crystallization of SnSe<sub>2</sub>, SnSe, and VSe<sub>2</sub> and all of these exhibited significant in-plane grain growth between 100 °C and 300 °C. The simultaneous formation of all three constituents suggests that the difference between the nucleation barriers for the three phases is small and controlled by the local Sn and Se composition.

#### CONCLUSIONS

In this work, in-plane diffraction measurements and Laue oscillations present in X-ray reflectivity scans of a designed precursor, as it evolved into a metastable heterostructure, enabled us to determine the absolute size of the growing crystal as a function of temperature. This data provided insights into the self-assembly mechanism and defined optimum processing conditions to form a new kinetically stable misfit layer compound, [(SnSe2)0.80]1(VSe2)1, with minimum oxidation. Controlling the local composition of the precursor enabled [(SnSe<sub>2</sub>)<sub>0.80</sub>]<sub>1</sub>(VSe<sub>2</sub>)<sub>1</sub> to preferentially form over [(SnSe)<sub>1.15</sub>]<sub>1</sub>(VSe<sub>2</sub>)<sub>1</sub>. Preparing a precursor with the same overall composition but different nanoarchitecture resulted in the formation of a new kinetically stable Sn<sub>x</sub>V<sub>1-x</sub>Se<sub>2</sub> alloy instead of [(SnSe<sub>2</sub>)<sub>0.80</sub>]<sub>1</sub>(VSe<sub>2</sub>)<sub>1</sub>. The different reactions encountered from annealing studies of closely related multilayer systems were discussed in terms of an energy landscape as an effort to rationalize the different self-assembly pathways observed. The results show that nanoarchitecture and local composition are complementary design parameters to direct the self-assembly of new kinetically stable compounds along different reaction pathways in the energy landscape.

## AUTHOR INFORMATION

## **Corresponding Author**

David C. Johnson — Department of Chemistry and Materials Science Institute, University of Oregon, Eugene, Oregon 97403, United States; ⊙ orcid.org/0000-0002-1118-0997; Email: davej@uoregon.edu

#### **Authors**

Dmitri Leo Mesoza Cordova — Department of Chemistry and Materials Science Institute, University of Oregon, Eugene, Oregon 97403, United States; orcid.org/0000-0002-7527-8950

- Taryn Mieko Kam Department of Chemistry and Materials Science Institute, University of Oregon, Eugene, Oregon 97403, United States
- Renae N. Gannon Department of Chemistry and Materials Science Institute, University of Oregon, Eugene, Oregon 97403, United States
- Ping Lu Sandia National Laboratories, Albuquerque, New Mexico 87185, United States

Complete contact information is available at: https://pubs.acs.org/10.1021/jacs.0c05505

#### **Notes**

This paper describes objective technical results and analysis. Any subjective views or opinions that might be expressed in the paper do not necessarily represent the views of the U.S. Department of Energy or the United States Government. The authors declare no competing financial interest.

## ACKNOWLEDGMENTS

The authors acknowledge support from the National Science Foundation under grant DMR-1710214. We also acknowledge the Center for Advanced Materials Characterization in Oregon (CAMCOR) at the University of Oregon. This work was performed, in part, at the Center for Integrated Nanotechnologies, an Office of Science User Facility operated for the U.S. Department of Energy (DOE) Office of Science by Los Alamos National Laboratory (contract DE-AC52-06NA25396) and Sandia National Laboratories (contract DE-NA-0003525).

## **■** REFERENCES

- (1) Trost, B. M.; Dong, G. Total Synthesis of Bryostatin 16 Using Atom-Economical and Chemoselective Approaches. *Nature* 2008, 456 (7221), 485–488.
- (2) Langmuir, I. The Arrangement of Electrons in Atoms and Molecules. J. Am. Chem. Soc. 1919, 41 (6), 868-934.
- (3) Pyykkö, P. Understanding the Eighteen-Electron Rule. J. Organomet. Chem. 2006, 691 (21), 4336–4340.
- (4) Wu, Y.; D'Agostino, C.; Holland, D. J.; Gladden, L. F. In Situ Study of Reaction Kinetics Using Compressed Sensing NMR. *Chem. Commun.* 2014, 50 (91), 14137–14140.
- (5) Capocasa, G.; Sessa, F.; Tavani, F.; Monte, M.; Olivo, G.; Pascarelli, S.; Lanzalunga, O.; Di Stefano, S.; D'Angelo, P. Coupled X-Ray Absorption/UV-Vis Monitoring of Fast Oxidation Reactions Involving a Nonheme Iron-Oxo Complex. J. Am. Chem. Soc. 2019, 141 (6), 2299–2304.
- (6) Huang, Z.; Dong, G. Site-Selectivity Control in Organic Reactions: A Quest To Differentiate Reactivity among the Same Kind of Functional Groups. Acc. Chem. Res. 2017, 50, 465–471.
- (7) Corey, E. J. The Logic of Chemical Synthesis: Multistep Synthesis of Complex Carbogenic Molecules (Nobel Lecture). *Angew. Chem., Int. Ed. Engl.* 1991, 30 (5), 455–465.
- (8) Disalvo, F. J. Solid-State Chemistry: A Rediscovered Chemical Frontier. Science (Washington, DC, U. S.) 1990, 247, 649-655.
- (9) Jansen, M. A Concept for Synthesis Planning in Solid-State Chemistry. *Angew. Chem., Int. Ed.* 2002, 41 (20), 3746–3766.
- (10) Pienack, N.; Bensch, W. In-Situ Monitoring of the Formation of Crystalline Solids. *Angew. Chem., Int. Ed.* 2011, 50 (9), 2014–2034.
- (11) Kanatzidis, M. G.; Pöttgen, R.; Jeitschko, W. The Metal Flux: A Preparative Tool for the Exploration of Intermetallic Compounds. *Angew. Chem., Int. Ed.* 2005, 44 (43), 6996–7023.
- (12) Xu, Y.; Musumeci, V.; Aymonier, C. Chemistry in Supercritical Fluids for the Synthesis of Metal Nanomaterials. *React. Chem. Eng.* 2019, 4 (12), 2030–2054.

- (13) Hagenmuller, P. Preparative Methods in Solid State Chemistry; Academic Press: New York, 1972.
- (14) Shoemaker, D. P.; Chung, D. Y.; Mitchell, J. F.; Bray, T. H.; Soderholm, L.; Chupas, P. J.; Kanatzidis, M. G. Understanding Fluxes as Media for Directed Synthesis: In Situ Local Structure of Molten Potassium Polysulfides. J. Am. Chem. Soc. 2012, 134 (22), 9456–9463.
- (15) Kohlmann, H. Looking into the Black Box of Solid-State Synthesis. Eur. J. Inorg. Chem. 2019, 2019 (39–40), 4174–4180.
- (16) Marbella, L. E.; Millstone, J. E. NMR Techniques for Noble Metal Nanoparticles. *Chem. Mater.* 2015, 27 (8), 2721–2739.
- (17) Mi, J. L.; Jensen, K. M. Ø.; Tyrsted, C.; Bremholm, M.; Iversen, B. B. In Situ Total X-Ray Scattering Study of the Formation Mechanism and Structural Defects in Anatase TiO<sub>2</sub> Nanoparticles under Hydrothermal Conditions. *CrystEngComm* 2015, 17 (36), 6868–6877.
- (18) Xu, H.; Sommer, S.; Broge, N. L. N.; Gao, J.; Iversen, B. B. The Chemistry of Nucleation: In Situ Pair Distribution Function Analysis of Secondary Building Units During UiO-66 MOF Formation. *Chem. Eur. J.* 2019, 25 (8), 2051–2058.
- (19) Bøjesen, E. D.; Jensen, K. M. Ø.; Tyrsted, C.; Mamakhel, A.; Andersen, H. L.; Reardon, H.; Chevalier, J.; Dippel, A. C.; Iversen, B. B. The Chemistry of ZnWO<sub>4</sub> Nanoparticle Formation. *Chem. Sci.* 2016, 7 (10), 6394–6406.
- (20) Bauers, S. R.; Wood, S. R.; Jensen, K. M. Ø.; Blichfeld, A. B.; Iversen, B. B.; Billinge, S. J. L.; Johnson, D. C. Structural Evolution of Iron Antimonides from Amorphous Precursors to Crystalline Products Studied by Total Scattering Techniques. *J. Am. Chem. Soc.* 2015, 137 (30), 9652–9658.
- (21) Bøjesen, E. D.; Iversen, B. B. The Chemistry of Nucleation. CrystEngComm 2016, 18 (43), 8332-8353.
- (22) Dippel, A.-C.; Bindzus, N.; Saha, D.; Delitz, J. T.; Liermann, H.-P.; Wahlberg, N.; Becker, J.; Bøjesen, E. D.; Brummerstedt Iversen, B. Synchrotron Powder Diffraction at P02.1 at PETRA III: From Electron Density Distributions to *in Situ* Total Scattering. *Z. Anorg. Allg. Chem.* 2014, 640 (15), 3094–3099.
- (23) Bayer, B. C.; Kaindl, R.; Monazam, M. R. A.; Susi, T.; Kotakoski, J.; Gupta, T.; Eder, D.; Waldhauser, W.; Meyer, J. C. Atomic-Scale in Situ Observations of Crystallization and Restructuring Processes in Two-Dimensional MoS<sub>2</sub> Films. *ACS Nano* 2018, 12 (8), 8758–8769.
- (24) Nielsen, M. H.; Aloni, S.; De Yoreo, J. J. In Situ TEM Imaging of CaCO<sub>3</sub> Nucleation Reveals Coexistence of Direct and Indirect Pathways. *Science (Washington, DC, U. S.)* 2014, 345 (6201), 1158–1162
- (25) Liu, C.; Malladi, S. K.; Xu, Q.; Chen, J.; Tichelaar, F. D.; Zhuge, X.; Zandbergen, H. W. In-Situ STEM Imaging of Growth and Phase Change of Individual CuAIX Precipitates in Al Alloy. *Sci. Rep.* 2017, 7 (1), 1–8.
- (26) West, A. R. Solid State Chemistry and Its Applications, 2nd ed.; John Wiley & Sons, Ltd: West Sussex, UK, 2014.
- (27) Lau, S. S.; Feng, J. S. Y.; Olowolafe, J. O.; Nicolet, M. A. Iron Silicide Thin Film Formation at Low Temperatures. *Thin Solid Films* 1975, 25 (2), 415–422.
- (28) Stein, A.; Keller, S. W.; Mallouk, T. E. Turning down the Heat: Design and Mechanism in Solid-State Synthesis. *Science (Washington, DC, U. S.)* 1993, 259 (5101), 1558–1564.
- (29) Chamorro, J. R.; Mcqueen, T. M. Progress toward Solid State Synthesis by Design. Acc. Chem. Res. 2018, 51, 2918-2925.
- (30) Schäfer, H. Preparative Solid State Chemistry: The Present Position. Angew. Chem., Int. Ed. Engl. 1971, 10 (1), 43-50.
- (31) De Yoreo, J.; Mandrus, D.; Soderholm, L.; Forbes, T.; Kanatzidis, M.; Wiesner, U.; Xu, T.; Tolbert, S.; Zawarotko, M.; Chan, J.; Mitchell, J.; Erlebacher, J.; Laskin, J.; Billinge, S.; Galli, G. Report of the Basic Energy Sciences Workshop on Synthesis Science for Energy Relevant Technology; US DOE, 2016.
- (32) Hamann, D. M.; Hadland, E. C.; Johnson, D. C. Heterostructures Containing Dichalcogenides-New Materials with

- Predictable Nanoarchitectures and Novel Emergent Properties. Semicond. Sci. Technol. 2017, 32 (9), 093004.
- (33) Hernan, L.; Morales, J.; Pattanayak, J.; Tirado, J. L. Preparation and Characterization of New Misfit Layer Selenides SnVSe 3 and SnNb 2 Se 5. *Chem. Lett.* 1991, 20 (11), 1981–1984.
- (34) Falmbigl, M.; Alemayehu, M. B.; Merrill, D. R.; Beekman, M.; Johnson, D. C. In-Plane Structure of Ferecrystalline Compounds. *Cryst. Res. Technol.* 2015, 50 (6), 464–472.
- (35) Bayard, M.; Sienko, M. J. Anomalous Electrical and Magnetic Properties of Vanadium Diselenide. *J. Solid State Chem.* 1976, 19, 325–329.
- (36) Evans, B. L.; Hazelwood, R. A. Optical and Electrical Properties of SnSe2. J. Phys. D: Appl. Phys. 1969, 2 (11), 1507-1516.
- (37) Cottrell, A. An Introduction to Metallurgy, 2nd ed.; Edward Arnold Publishers, Ltd.: London, UK, 1975.
- (38) Fister, L.; Li, X.; McConnell, J.; Novet, T.; Johnson, D. C. Deposition System for the Synthesis of Modulated, Ultrathin-film Composites. J. Vac. Sci. Technol., A 1993, 11 (6), 3014–3019.
- (39) Hamann, D. M.; Bardgett, D.; Cordova, D. L. M.; Maynard, L. A.; Hadland, E. C.; Lygo, A. C.; Wood, S. R.; Esters, M.; Johnson, D. C. Sub-Monolayer Accuracy in Determining the Number of Atoms per Unit Area in Ultrathin Films Using X-Ray Fluorescence. *Chem. Mater.* 2018, 30 (18), 6209–6216.
- (40) Toby, B. H.; Von Dreele, R. B. GSAS-II: The Genesis of a Modern Open-Source All Purpose Crystallography Software Package. *J. Appl. Crystallogr.* 2013, 46 (2), 544–549.
- (41) Rodríguez-Carvajal, J. FULLPROF: A Program for Rietveld Refinement and Pattern Matching Analysis. In Abstracts of the Satellite Meeting on Powder Diffraction of the XV Congess of the IUCr, Toulouse, France, 1990; p 127.
- (42) Schneemeyer, L. F.; Stacy, A.; Sienko, M. J. Effect of Nonstoichiometry on the Periodic Lattice Distortion in Vanadium Diselenide. *Inorg. Chem.* 1980, 19 (9), 2659–2662.
- (43) Holy, V.; Pietsch, U.; Baumbach, T. High-Resolution X-Ray Scattering from Thin Films and Multilayers; Springer Berlin Heidelberg: Germany, 1999.
- (44) Stierle, A.; Vlieg, E. Surface Sensitive X-Ray Diffraction Methods. In *Modern Diffraction Methods*; Mittemeijer, E. J., Welsel, U., Eds.; Wiley-VCH Verlag & Co.: Weinheim, Germany, 2013; pp 221–258
- (45) Woolfson, M. M. An Introduction to X-Ray Crystallography, 2nd ed.; Cambridge University Press: Cambridge, UK, 1997.
- (46) Callister, W. D. J.; Rethwisch, D. G. Materials Science and Engineering: An Introduction, 8th ed.; John Wiley and Sons Inc.: Hoboken, NJ, 2010.
- (47) Shimada, T.; Ohuchi, F. S.; Parkinson, B. A. Thermal Decomposition of SnS <sub>2</sub> and SnSe <sub>2</sub>: Novel Molecular-beam Epitaxy Sources for Sulfur and Selenium. *J. Vac. Sci. Technol., A* 1992, 10 (3), 539–542.
- (48) Cordova, D. L. M.; Kam, T. M.; Fender, S. S.; Tsai, Y. H.; Johnson, D. C. Strong Non-Epitaxial Interactions: Crystallographically Aligned PbSe on VSe<sub>2</sub>. *Phys. Status Solidi A* 2019, 216 (15), 1800896.
- (49) Atkins, R.; Disch, S.; Jones, Z.; Haeusler, I.; Grosse, C.; Fischer, S. F.; Neumann, W.; Zschack, P.; Johnson, D. C. Synthesis, Structure and Electrical Properties of a New Tin Vanadium Selenide. *J. Solid State Chem.* 2013, 202, 128–133.
- (50) Beekman, M.; Rodriguez, G.; Atkins, R.; Kunert, J.; Moore, D. B.; Johnson, D. C. Detection of Nanoscale Embedded Layers Using Laboratory Specular X-Ray Diffraction. *J. Appl. Phys.* 2015, 117 (18), 185306.
- (51) Atkins, R.; Dolgos, M.; Fiedler, A.; Grosse, C.; Fischer, S. F.; Rudin, S. P.; Johnson, D. C. Synthesis and Systematic Trends in Structure and Electrical Properties of  $[(SnSe)_{1.15}]_m(VSe_2)_1$ , m=1, 2, 3, and 4. Chem. Mater. 2014, 26 (9), 2862–2872.
- (52) Björck, M.; Andersson, G. GenX: An Extensible X-Ray Reflectivity Refinement Program Utilizing Differential Evolution. *J. Appl. Crystallogr.* 2007, 40 (6), 1174–1178.

- (53) Hite, O. K.; Falmbigl, M.; Alemayehu, M. B.; Esters, M.; Wood, S. R.; Johnson, D. C. Charge Density Wave Transition in  $(PbSe)_{1+\delta}(VSe_2)_n$  Compounds with n=1, 2, and 3. *Chem. Mater.* 2017, 29 (13), 5646–5653.
- (54) Hite, O. K.; Nellist, M.; Ditto, J.; Falmbigl, M.; Johnson, D. C. Transport Properties of VSe<sub>2</sub> Monolayers Separated by Bilayers of BiSe. *J. Mater. Res.* 2016, 31 (7), 886–892.
- (55) Hadland, E.; Jang, H.; Falmbigl, M.; Fischer, R.; Medlin, D. L.; Cahill, D. G.; Johnson, D. C. Synthesis, Characterization, and Ultralow Thermal Conductivity of a Lattice-Mismatched SnSe<sub>2</sub>(MoSe<sub>2</sub>)<sub>1,32</sub> Heterostructure. *Chem. Mater.* 2019, 31 (15), 5699-5705.
- (56) Van Aert, S.; Verbeeck, J.; Erni, R.; Bals, S.; Luysberg, M.; Van Dyck, D.; Van Tendeloo, G. Quantitative Atomic Resolution Mapping Using High-Angle Annular Dark Field Scanning Transmission Electron Microscopy. *Ultramicroscopy* 2009, 109 (10), 1236–1244.
- (57) Hamann, D. M.; Merrill, D. R.; Bauers, S. R.; Mitchson, G.; Ditto, J.; Rudin, S. P.; Johnson, D. C. Long-Range Order in [(SnSe)<sub>1,2</sub>]<sub>1</sub>[TiSe<sub>2</sub>]<sub>1</sub> Prepared from Designed Precursors. *Inorg. Chem.* 2017, 56 (6), 3499–3505.
- (58) Falmbigl, M.; Putzky, D.; Ditto, J.; Esters, M.; Bauers, S. R.; Ronning, F.; Johnson, D. C. Influence of Defects on the Charge Density Wave of  $([SnSe]_{1+\delta})_1(VSe_2)_1$  Ferecrystals. *ACS Nano* 2015, 9 (8), 8440–8448.
- (59) Westover, R.; Atkins, R. A.; Falmbigl, M.; Ditto, J. J.; Johnson, D. C. Self-Assembly of Designed Precursors: A Route to Crystallographically Aligned New Materials with Controlled Nanoarchitecture. *J. Solid State Chem.* 2016, 236, 173–185.
- (60) Falmbigl, M.; Esters, M.; Johnson, D. C. Formation of a Selenide-Based Heterostructure From a Designed Precursor<sup>†</sup>. *Cryst. Res. Technol.* 2017, 52 (10), 1700067.